

1 **Simultaneous OI 630 nm imaging observations of thermospheric gravity waves and**  
2 **associated revival of fossil depletions around midnight near the EIA crest**

3  
4  
5 **Authors:**

6 **1. Navin Parihar**

7 Indian Institute of Geomagnetism, Navi Mumbai, India

8 e-mail: [navindeparihar@gmail.com](mailto:navindeparihar@gmail.com)

9  
10 **2. Saranya Padincharapad**

11 (a) Equatorial Geophysical Research Laboratory, Indian Institute of Geomagnetism,  
12 Tirunelveli, India

13 (b) Manonmaniam Sundaranar University, Tirunelveli, India

14 e-mail: [anuja8494@gmail.com](mailto:anuja8494@gmail.com)

15  
16 **3. Anand Kumar Singh**

17 National Centre for Polar and Ocean Research, Goa, India

18 e-mail: [singhaaks@gmail.com](mailto:singhaaks@gmail.com)

19  
20 **4. Prasanna Mahavarkar**

21 Indian Institute of Geomagnetism, Navi Mumbai, India

22 e-mail: [mahavarkarprasanna@gmail.com](mailto:mahavarkarprasanna@gmail.com)

23  
24 **5. A. P. Dimri**

25 Indian Institute of Geomagnetism, Navi Mumbai, India

26 e-mail: [apdimri@hotmail.com](mailto:apdimri@hotmail.com)

27  
28 **Corresponding Author:**

29 **Navin Parihar**, Indian Institute of Geomagnetism, Navi Mumbai, India

30 e-mail: [navindeparihar@gmail.com](mailto:navindeparihar@gmail.com)

31  
32 **Key Words:**

33 Airglow imaging; Midnight Irregularities/Depletions; Gravity wave seeding; Low-  
34 latitude ionosphere.

36 **Abstract**

37 We report the F-region airglow imaging of fossil plasma depletions around midnight that  
38 revived afresh under the persisting thermospheric gravity wave (GW) activity. An all-sky  
39 imager recorded these events in OI 630 nm imaging over Ranchi (23.3° N, 85.3° E, mlat. ~19°  
40 N), India, on 16 April 2012. Northward propagating and east-west aligned GWs ( $\lambda$  ~210 km,  
41  $v$  ~64 m/s, and  $\tau$  ~0.91 h) were seen around midnight. Persisting for ~2 hours, this GW  
42 activity revived two co-existing and eastward drifting fossil depletions, DP1 and DP2. GWs-  
43 driven revival was prominently seen in depletion DP1, wherein its apex height grew from  
44 ~600 km to >800 km, and the level of intensity depletion increased from ~17% to 50%.  
45 Present study is novel in the sense that simultaneous observations of thermospheric GWs  
46 activity and associated evolution of depletion in OI 630 nm airglow imaging, and that too  
47 around local midnight, have not been reported earlier. Current understanding is that GW  
48 phase fronts aligned parallel to the geomagnetic field lines and eastward propagating are  
49 more effective in seeding Rayleigh-Taylor (RT) instability. Here, GW fronts were east-west  
50 aligned (i.e. perpendicular to the geomagnetic field lines) and propagated northward, yet they  
51 revived fossil depletions.

52

53

## 54 1. Introduction

55 Gravity waves (GWs) are well-known to influence the mesosphere-lower thermosphere-  
56 ionosphere (MLTI) region. GWs significantly contribute to the momentum and energy budget  
57 of the MLT region via the wave-dissipation processes (Fritts and Alexander, 2003; Holton,  
58 1983). Apart from the dominant solar and geomagnetic inputs, GWs are the key element in  
59 some of the electrodynamic processes in the ionosphere e.g. irregularities, atmosphere-  
60 ionosphere (AI) coupling, traveling ionospheric disturbances, etc.. In the equatorial F-region,  
61 GWs modulate the ionospheric plasma into wave-like ionization structures. Under favourable  
62 conditions, these structures act as a seed to Generalized Rayleigh-Taylor (GRT) instability  
63 that generates the irregularities (Fritts et al., 2009; Huba and Joyce, 2007, 2010; Huba and  
64 Liu, 2020; Hysell et al., 1990; Kelley, 2009; Woodman, 2009). GWs are also important in the  
65 AI coupling during deep convection activity, thunderstorms, lightning, cyclones, tornadoes,  
66 transient luminous events (TLEs)/sprites initiation, tsunamis, etc. (Azeem and Barlage, 2018;  
67 Maurya et al., 2022; Huba et al., 2015). GWs can also generate medium-scale traveling  
68 ionospheric disturbances (MSTIDs) (Fukushima et al., 2012; Figueiredo et al., 2018; Heale et  
69 al., 2022, and references cited therein). On the course of their propagation, GWs can also  
70 induce periodic fluctuations in the ionospheric parameters e.g. the electron density or total  
71 electron content (TEC), the F-region height, temperatures and winds, etc. (Ford et al., 2006,  
72 2008; Klausner et al., 2009; Parihar et al., 2018; Vadas and Azeem, 2021) or airglow  
73 emission (Huba et al., 2015; Makela et al., 2011).

74

75 The crucial role of GWs in seeding the post-sunset equatorial spread-F (ESF) or plasma  
76 bubbles (EPBs) is fairly well understood (Abdu et al., 2009; Fritts et al., 2009; Huba and  
77 Joyce, 2007, 2010; Hysell et al., 1990; Kelley, 2009; Singh et al., 1997; Tsunoda, 2010;  
78 Tulasi Ram et al., 2014; Woodman, 2009). However, their role in the seeding of the  
79 midnight/post-midnight irregularities remains poorly understood, especially when the  
80 important criteria for the triggering of the GRT instability are absent (e.g., the favorable  
81 alignment of the solar terminator with the geomagnetic field lines and the pre-reversal  
82 enhancement, PRE, of the zonal electric field). Lately, Huba and Liu (2020) reported the  
83 global simulations of the ESF using the SAMI3/WACCM-X coupled model. SAMI3 is the  
84 abbreviation for ‘*Sami3 is Another Model of Ionosphere*’ (Huba et al., 2008), and WACCM-  
85 X stands for the ‘*Whole Atmosphere Community Climate Model with thermosphere and*  
86 *ionosphere extension*’ (Liu et al., 2010). For the first time, Huba and Liu’s (2020) simulations  
87 demonstrated that GWs are the dominant seed mechanism and can spontaneously generate

88 the ESF, and that the EPBs develop self-consistently in the postsunset ionosphere. Studies by  
89 Nishioka et al. (2012) show that the GRT instability can occur near midnight under the  
90 influence of enhanced GW activity and then can lead to the growth of irregularities. MSTIDs  
91 are an important generation mechanism of post-midnight irregularities wherein the electric  
92 field perturbations associated with them acts as the seed (Miller et al., 2009; Taori et al.,  
93 2015). Otsuka (2018) have presented an elaborative review of these mechanisms. All-sky  
94 airglow imaging (ASAI) along with the radar, ionosonde, and GPS measurements have  
95 significantly contributed to our understanding of the crucial role of GWs in seeding the EPBs  
96 (Mendillo and Baumgardner, 1982; Mendillo et al., 1997; Taori et al., 2010; Yadav et al.,  
97 2017). *Spread-F Experiment (SpreadFEx)* carried out in Brazil during September-November  
98 2005 is one such example (Fritts et al., 2009). In the Indian subcontinent, Sreeja et al. (2009)  
99 reported the GWs in OI 630 nm dayglow intensity variations that acted as a seed to the ESF  
100 irregularities.

101

102 GWs that give rise to the EPBs have usually been reported in the MLT region airglow  
103 imaging (e.g. Fritts et al., 2009; Paulino et al., 2011; Takahashi et al., 2009; Taori et al.,  
104 2013). Reports featuring them in the F-region airglow imaging are rare and limited to that of  
105 Makela et al. (2011), Paulino et al. (2016, 2018), Sau et al. (2018), and Smith et al. (2015).  
106 Makela et al. (2011) and Smith et al. (2015) reported the thermospheric imaging observations  
107 of GWs associated with tsunami and earthquake, respectively. Paulino et al. (2016, 2018) and  
108 Sau et al. (2018) presented their observations in OI 630 nm imaging from Brazil and India,  
109 respectively. However, these authors did not report any occurrence of depletions during the  
110 undergoing GW activity. We report, for the first time, simultaneous observations GWs and  
111 depletions in the F-region airglow imaging.

112

113 On the course of temporary campaign-based ASAI observations of OI 630 nm emission  
114 under *Climate And Weather of Sun-Earth System (CAWSES) India Phase II Programme*  
115 at Ranchi (23.3° N, 85.3° E, mlat. ~19° N), GW activity and “fossil depletions” were seen  
116 together on 16 April 2012 with the former reviving the latter. Fossil depletions are the  
117 remnants of airglow depletion or EPBs that have ceased growing upward or poleward;  
118 however, they continue to persist and move with ambient plasma drift. Under *Maui Middle*  
119 *Atmosphere and Lower Thermosphere (Maui-MALT)* initiative, Makela et al. (2004) reported  
120 their extensive observations in OI 630 nm imaging from Haleakala Volcano (20.7° N, 203.7°  
121 E; mlat. 21.3° N), Hawaii during the solar maximum of 2002-2003. Chapagain et al. (2011)

122 presented their limited observations from Christmas Island ( $2.1^{\circ}$  N,  $157.4^{\circ}$  W, mlat.  $2.8^{\circ}$  N)  
123 during September 1995. In India, Sekar et al. (2007) presented their case study from Gadanki  
124 ( $13.5^{\circ}$  N,  $79.2^{\circ}$  E, mlat.  $6.3^{\circ}$  N). However, these investigations did not discuss any  
125 resurgence of fossil depletions associated with the GW activity. Novelty of this study is that  
126 the “fossil depletions” revived into “active depletions” after the emission layer witnessed the  
127 GW activity. Lately, Wrasse et al. (2021) presented an interesting event wherein a fossil EPB  
128 merged with other ones after interacting with an electrified MSTID and turned into an active  
129 bubble.

130

131

## 132 **2. Instrumentation and data**

133 Under the *CAWSES India Phase II Programme*, an ASAI was installed for limited  
134 nightglow observations at Ranchi ( $23.3^{\circ}$  N,  $85.3^{\circ}$  E, mlat.  $\sim 19^{\circ}$  N), located near the crest of  
135 equatorial ionization anomaly (EIA) in India during April 2012. Parihar et al. (2017) and  
136 Parihar (2019) have described this ASAI system in detail. OI 630 nm emission was  
137 monitored using a 2.2 nm half-power bandwidth optical filter having transmittance of  $\sim 77\%$ .  
138 Our imager’s field-of-view roughly covered about  $7\text{--}8^{\circ}$  latitude/longitude region at 250 km  
139 over Ranchi. Airglow images were flat-fielded to reduce the inhomogeneous contribution at  
140 lower elevations due to van Rhijn effect and non-uniform sensitivity of CCD detector at  
141 different pixels. Next, following the technique described by Wrasse et al. (2021), we  
142 detrended the individual images to enhance the contrast of airglow features using an hour  
143 running average image. Using known astral positions and assuming OI 630 nm emission peak  
144 at 250 km, the geographic coordinates of each pixel was determined following the technique  
145 of Garcia et al. (1997). Using this information, all-sky images were unwarped. We follow the  
146 technique discussed by Pimenta et al. (2003) to determine the drift velocity of depletions.  
147 First, for a given latitude, two intensity profiles along east-west direction as a function of  
148 distance was generated using two successive unwarped images. Next, the east-west  
149 displacement of depletion was estimated using these two profiles from which drift speed was  
150 determined (see Pimenta et al., 2003 for details of this technique). Similarly, the propagation  
151 characteristics of GW fronts were estimated by tracking faint crest and trough along the  
152 propagation direction in the consecutive images. As GW fronts were unclear in images, we  
153 used contrast-enhanced images. We, also, generated NS keograms to visualize GW traces and  
154 determine their speed. A keogram is a time-versus-latitude plot generated by extracting a NS  
155 column from individual images and stacking them horizontally. Next, GWs speed was, also,

156 estimated from the slope of wave traces seen in these keograms (Makela et al., 2006). We  
157 looked into the total electron content (TEC) measurements from an *International GNSS*  
158 *Service* station Hyderabad (17.3° N, 78.6° E, mlat. ~12.0° N, located nearby and south of  
159 Ranchi) to ascertain GW activity seen in the ASAI observations (Source: <https://t-ict4d.ictp.it/nequick2/gnss-tec-calibration>,  
160 Ciruolo et al., 2007). Quiet geomagnetic  
161 conditions prevailed on this night with  $Kp < 2$ ,  $Ap = 4$ , and  $-4 < Dst < 10$  nT.

162  
163

### 164 3. Observations

165 Such GWs-driven revival of “fossil depletions” was recorded in airglow images during 1700-  
166 2000 UT on 16 April 2012. Here, Indian Standard Time (IST) = Universal Time (UT) + 0530  
167 and Local Time (LT)  $\approx$  IST. As such, 1700-2000 UT corresponds to  $\sim$ 1.5 h duration before  
168 and after the local midnight. Figures 1 and 2 present airglow images that depict this event  
169 seen over Ranchi during 1742-1942 UT on 16 April 2012. As the faint airglow features were  
170 getting lost in the unwarping process, warped all-sky images are presented. Supplementary  
171 material S1 shows the movie created from these images that feature this event. Fossil  
172 depletions of our interest that showed the GWs-driven revival are marked as **DP1** and **DP2** in  
173 Figure 1 and 2. Here, **ROI1** is the region-of-interest wherein a few weakly perceivable fronts  
174 of GWs and fossil depletions coexisted initially.

175

#### 176 3.1 Signatures of GW activity in the F-region

177 We first observed faint signatures of GW activity near the southern edge of the field-of-view  
178 (FOV) during  $\sim$ 1715-1724 UT. Successive images showed unclear signatures of GWs  
179 activity. Starting  $\sim$ 1730 UT, their presence became more evident and continued until 1906  
180 UT or so. GWs fronts were not clearly seen because of their interaction with co-existing  
181 depletions. Some weakly perceivable bright fronts are marked as ‘f1’, ‘f2’, ‘f3’ and ‘f4’ in  
182 Figure 1 and 2. Similarly, dark trough that precede fronts ‘f1’ and ‘f2’ are marked as ‘t1’ and  
183 ‘t2’, respectively. Often GWs in OI 630 nm imaging are faint and unclear. Under similar  
184 situations, Makela et al. (2011) found that time difference (TD) images have proven ability to  
185 reflect such GWs faint fronts. In their work, initial analysis of raw images did not show any  
186 GWs activity linked with tsunamis; however, TD images indeed reflected associated GWs. We  
187 generated such TD images and are shown in Figure 3 which clearly show dark troughs ‘t1’  
188 and ‘t2’ and GW fronts ‘f1’ and ‘f2’. North-south (NS) keograms [shown in Figure 4 (a) and

189 (b)] showed a few clear alternating bright and dark intensity striations over the north, and  
190 their slope indicates that GWs propagated towards the north. We estimated GWs propagation  
191 characteristics using the slope of wave traces (marked by black arrow 'b1', 'b2', 'b3', 'b4') in  
192 keograms and cross-verified them with the intensity profiling technique. We found that these  
193 GWs propagated from the south to north with the phase speed ( $v$ ) of  $\sim 64 \pm 2$  m/s and had the  
194 horizontal wavelength ( $\lambda$ ) and period ( $\tau$ ) of  $\sim 210 \pm 6$  km and  $\sim 0.91 \pm 0.06$  h, respectively.

195

196 We further looked into the TEC measurements from IGS station Hyderabad ( $17.3^\circ$  N,  $78.6^\circ$   
197 E, mlat.  $\sim 12.0^\circ$  N), India to confirm this on-going GWs activity. Figure 5 shows the TEC  
198 measurements depicting GW activity in and around Hyderabad during 1700-2000 UT on this  
199 night. Figure 5 (a) shows the scatter plots of the TEC along the trajectory of ionospheric  
200 pierce points (IPPs) for different GPS satellites during 1700-1930 UT on this night. PRN  
201 numbers of GPS satellites, along with the start time at 1700 UT, are indicated next to the  
202 corresponding IPPs trajectory. TEC variations along the NS-aligned IPPs tracks (e.g. G27  
203 and G28) clearly show the wavelike fluctuations in the  $15$ - $20^\circ$  N latitude range. The temporal  
204 evolution of the TEC for a few satellites is shown in Figure 5 (b). Of our interest is G28's  
205 TEC measurement as its IPPs trajectory lay close to the imager's ROI1 during 1700-1800 UT  
206 which showed a strong signature of GWs. By performing the periodogram analysis of the  
207 temporal and spatial variation of its TEC, we estimated the propagation characteristics of GW  
208 to be  $\tau \sim 0.95 \pm 0.03$  h,  $\lambda \sim 229 \pm 12$  km, and  $v \sim 67 \pm 5$  m/s, and is in good agreement with the  
209 ASAI observations. Further, the propagation direction of GWs seen in airglow imaging is in  
210 good agreement with these previous reports. Studies on the GW activity at the MLT heights  
211 over a farther low-latitude station Prayagraj ( $25.5^\circ$  N, formerly Allahabad) in India showed  
212 their propagation either northward or northeast around midnight during April-May  
213 (Mukherjee et al., 2010). A comprehensive study of thermospheric GWs in the ASAI  
214 observations over Tirunelveli ( $8.7^\circ$  N) in India during 2013-2015 indicated their propagation  
215 toward the north-northwest during the equinoxes (Sau et al., 2018).

216

### 217 **3.2 GWs-driven revival of fossil depletions**

218 During 1730-1748 UT, faint signatures of depletion DP1 that revived were seen in the ROI1.  
219 Depletion DP1 lacked any poleward growth during 1730-1806 UT. Using the equation given  
220 in Kelley (2009) and by tracking the poleward tip of depletion, we estimated the apex height  
221 of the associated geomagnetic flux tubes ( $A_H$ ) and found it to be steady at  $\sim 600$  km. Within it,

222 the level of intensity reduction with respect to that of the ambient region (i.e.,  $\Delta I/I_{\text{ambient region}}$ )  
223 was  $\sim 17\%$ . However, depletion DP1 drifted gradually to the east with a speed of 59-70 m/s.  
224 Beginning 1812-1818 UT, this depletion started to intensify steadily, gain contrast against the  
225 background and become noticeable. Southern end of depletion DP1 was fused with that of a  
226 preceding depletion OD2. A few faint NS-aligned depletions were also present in the ROI1.  
227 Along with depletion DP1, they intersected the EW-aligned fronts 'f1' and 'f2' of GWs, and  
228 fragmented them into few isolated structures. Later on, these structures got attached to the  
229 west wall of depletion DP1 and started moving in unison. Clear signs of two such fragments  
230 (marked as S1 and S2 in Figure 1 and 2) can be seen at  $\sim 1830$  UT and  $\sim 1806$ -1812 UT,  
231 respectively. Starting 1824-1830 UT, we noted airglow enhancement to occur near its east  
232 wall that then started to become distinct. As a result, an *inverted arrowhead*-shaped depletion  
233 with an unusually wide southern fraction was evident during 1836-1854 UT. As two attached  
234 structures S1 and S2 drifted along with depletion DP1, they tilted considerably to the east by  
235  $\sim 60$ - $75^\circ$  (see the ASAI images beginning 1830 UT in Figures 1 and 2). At  $\sim 1900$  UT, the  
236 structure S1 was almost aligned and merged with the west wall of depletion DP1, which led  
237 to a fairly distinct west wall (seen as weak airglow enhancement). Airglow enhancement near  
238 both the east and west wall (marked as A1 and A2, respectively, in Figure 2) continued, and a  
239 linear NS-aligned depletion DP1 (having  $A_H > 800$  km and  $\Delta I/I_{\text{ambient region}} \sim 50\%$ ) was seen at  
240 1906-1912 UT. Within the next 6-12 min, the apex of structure S2 merged with airglow  
241 enhancement A2 near the west wall.

242

243 Next, some airglow enhancement occurred in the inner edge of the west wall of depletion  
244 DP1 at 1924 UT (see the region-of-interest, ROI2 in Figure 2). We interpret this as a  
245 consequence of some ambient plasma intrusion across its west wall. Later, such intrusion led  
246 to the disappearance of its southern fraction and the formation of an isolated depletion at  
247 1942 UT. Possibly these disappearances occurred due to the filling of the EIA plasma into  
248 depletion across its western wall (see Otsuka et al., 2012). Similarly, fossil depletion DP2  
249 also revived; however, its evolution was much simpler than that of depletion DP1.

250

#### 251 **4 Discussions**

252 We present rare simultaneous observations of GWs activity and associated revival of fossil  
253 depletions in the F-region airglow imaging around midnight over an off-equatorial station  
254 Ranchi (located near the EIA crest) in India. Post-sunset ionospheric irregularities, in the



255 equatorial region, are generated by the GRT instability that sets off under the suitable  
256 combination of (i) favourable alignment of solar terminator with geomagnetic field lines; (ii)  
257 rapid height rise of the F-layer; (iii) absence of strong transequatorial wind and (iv) necessary  
258 seed perturbation (Fejer and Kelley, 1980; Kelley, 2009; Makela and Otsuka, 2012;  
259 Woodman, 2009). Stronger the height rise of the F-layer and an initial seed perturbation is,  
260 the faster the growth rate of GRT instability, which ultimately leads to the rapid evolution of  
261 the irregularities (Huba and Joyce, 2007; Huang et al., 1993; Hysell et al., 2014; Kelley et al.,  
262 1981; Krall et al., 2013; Tsunoda, 2010; Zalesak and Ossakow, 1980). GWs are well known  
263 to deform the bottom side plasma of the F-region into the wavelike ionization structures that  
264 then act as a seed to GRT instability, which, in turn, generates irregularities (Kelley et al.,  
265 1981; Hysell et al., 1990; Huba and Liu, 2020). While their role in the generation of the post-  
266 sunset irregularities is well known, our understanding is limited in the context of  
267 midnight/post-midnight irregularities. Present study features midnight fossil airglow  
268 depletions that revived due to undergoing GW activity and turned into an active depletion.

269

270 Northward propagating GWs having  $\lambda \sim 210$  km,  $v \sim 64$  m/s, and  $\tau \sim 0.91$  h were recorded in  
271 630 nm nightglow images during 1715-1906 UT. Supporting airglow observations, TEC  
272 measurements, too, showed the presence of similar GWs. Simultaneously, an eastward  
273 drifting fossil depletion DP1 ( $A_H \sim 600$  km and  $\Delta I/I_{\text{ambient region}} \sim 17\%$ ) co-existed during  
274 1730-1748 UT. Next, depletion DP1 and other co-existing depletions intercepted EW-aligned  
275 GW fronts and fragmented them during 1806-1824 UT. Subsequently, two such fragments  
276 viz. S1 and S2 that lay close to depletion DP1 got attached to its west wall, started drifting  
277 eastward in unison, tilted significantly to the east, and almost got aligned with the west wall.  
278 Next, depletion DP1 gradually intensified, surged polewards, and became a well-developed  
279 linear depletion ( $A_H > 800$  km and  $\Delta I/I_{\text{ambient region}} \sim 50\%$ ) during 1906-1912 UT. Meanwhile,  
280 airglow enhancement continued to develop near both its walls and an uneven broadening was  
281 seen in its southern half. Next, some ambient plasma diffusion occurred near this uneven  
282 region leading to airglow enhancement in the inner edge of its west wall at 1924 UT. Such  
283 intrusion continued, its southern fraction gradually disappeared, and an isolated depletion was  
284 formed at 1942 UT. Present observations clearly indicate that “fossil depletion” DP1 revived  
285 and became an “active depletion” under the influence of co-existing GWs activity. Another  
286 succeeding depletion, DP2, too, showed a similar revival.

287

288 An important consideration in the GWs seeding of the GRT instability is the alignment of  
289 their wavefronts with the geomagnetic field lines. The current understanding is that the  
290 strength of the polarization electric field generated by the GWs greatly depends on the angle  
291 between them, and the maximum polarization occurs when their wavefront is aligned with the  
292 geomagnetic field (Huba et al., 2015; Hysell et al., 2014; Krall et al., 2013; Tulasi Ram et al.,  
293 2014; Tsunoda, 2010). Numerical simulations by Hysell et al. (2014) suggest that the GWs-  
294 induced modulations were the most severe when their fronts were aligned with the magnetic  
295 meridian. Using Communications/Navigation Outrage Forecasting System (C/NOFS) mission  
296 TEC measurements, Tulasi Ram et al. (2014) studied the characteristics of large-scale wave  
297 structure (LSWS) at the base of the F-region and their association with the EPBs occurrences  
298 in Southeast Asia and Africa. Authors found that the EPBs frequently occurred when the  
299 amplitudes of LSWS were adequately increased, and their phase fronts were geomagnetic  
300 field-aligned.

301

302 In the present study, the GWs fronts were east-west aligned (i.e., transverse to the  
303 geomagnetic field lines) and propagated northward. Yet, fossil depletions DP1 and DP2  
304 revived and is intriguing. Meridional wind perturbations associated with GWs are known to  
305 be ineffective in the initiation and development of depletions. Present observations are in  
306 contrast with this notion and point towards another excitation mechanism rather than GRT  
307 instability, which we conjecture, is the spatial resonance mechanism for these reasons. Good  
308 matching was seen between the GWs phase speed ( $v \sim 64-67$  m/s) and the eastward drift of  
309 depletion DP1 ( $v \sim 59-70$  m/s). Horizontal Wind Model 2007 estimates also indicated the  
310 zonal thermospheric wind speed of 51-61 m/s (Drob et al., 2008). We estimated the speed at  
311 which the apex of DP1 progressed poleward and found it to be in the range of 46-56 m/s.  
312 Spatial resonance theory of GWs seeding of irregularities states that the effects of GWs  
313 perturbations are the strongest when its phase speed and the plasma drift velocity are nearly  
314 equal (Kelley et al., 1981). Under such conditions, the ionospheric plasma exerts the GW-  
315 associated forcing for a longer duration; thereby, accelerating the formation of ionization  
316 structures. As such, we conjecture that this GWs-driven revival of fossil depletions occurred  
317 via the spatial resonance mechanism. Numerical simulations by Huang and Kelley (1996)  
318 suggest that this mechanism can accelerate the formation of depletions. Possibly continuously  
319 undergoing GWs activity for 2 hours in the F-region sufficiently intensified the magnitude of

320 associated ionization modulations, which in turn triggered and sustained the revival of fossil  
321 depletions via the spatially resonant mechanism.

322

323 Similar event of GWs associated revival of a fossil depletion occurred around midnight on 06  
324 March 2013 as well and is shown in Figure 6. On this night, GW activity persisted during  
325 1530-1745 UT and concerned fossil depletion **DP3** revived during 1730-1854 UT. Typical  
326 ASAI images showing the signs of GW activity are presented in Figure 7. During 1636-1736  
327 UT, GWs had  $\lambda \sim 196 \pm 4$  km,  $v \sim 160 \pm 4$  m/s and  $\tau \sim 0.34 \pm 0.02$  h, propagated from SW-  
328 NE, and their fronts were  $\sim 74^\circ$  aligned with the geomagnetic field line. First, the southern  
329 fraction of depletion **DP3** drifted into the western edge of the FOV at 1706-1712 UT. Later,  
330 this depletion was seen as an isolated linear depletion during 1730-1736 UT confined within  
331 the  $\sim 20.1$ - $23.2^\circ$  N latitude regime with NS extension of  $\sim 480 \pm 18$  km. On course of its  
332 eastward drift, depletion **DP3** gradually intensified and developed both poleward and  
333 equatorward. During 1706-1800 UT, its base swiftly surged equatorward approximately from  
334  $20.2^\circ$  to  $17.7^\circ$  N. Comparatively, its poleward growth was slower. When well-developed at  
335 1900 UT, its NS extension was in  $17$ - $26^\circ$  N latitudes (i.e. greater than  $980 \pm 22$  km).  
336 Simultaneously, two structuring **BR1** and **BR2** developed on its east wall and an isolated  
337 depletion (**ID1**) lay on its east at  $\sim 20.5^\circ$  N latitude. We found its drift speed to be in the 81-  
338 109 m/s range.

339

340 Meridional wind can influence the growth rate of GRT instability by altering the field-line  
341 integrated Pederson conductivity. Maruyama (1988) and Abdu et al. (2006) found that strong  
342 meridional winds could reduce the growth rate of RTI and suppress irregularities. Huba and  
343 Krall (2013) have reported both stabilizing and destabilizing effects of the meridional winds  
344 on RT instability. Devasia et al. (2002) found that a suitable combination of the meridional  
345 wind and F-region base height favours ESF development. In the present study, the meridional  
346 wind measurements using a Fabry-Perot interferometer, etc. were not available; hence, their  
347 possible role in the evolution of these fossil depletions could not be investigated.

348

349 We know that the electric field perturbations associated with MSTIDs can influence the  
350 growth of irregularities. Otsuka et al. (2012) and Shiokawa et al. (2015) reported the  
351 disappearance of an EPB upon interaction with MSTIDs and large-scale traveling ionospheric  
352 disturbances (LSTIDs), respectively. Authors suggested that the electric field associated with

353 MSTIDs/LSTIDs can move ambient plasma into the bubble across the geomagnetic field line  
354 through  $\mathbf{E} \times \mathbf{B}$  drift which will result in the filling and subsequent disappearance of the  
355 depletion. Studies by Miller et al. (2009), Taori et al. (2015) and Takahashi et al. (2020)  
356 suggest that MSTIDs can directly seed EPBs. Simulation studies by Krall et al. (2011),  
357 further, indicates that the electric field associated with electrified MSTIDs can enhance the  
358 growth of EPBs. Lately, Wrasse et al. (2021) presented an interesting observations of the  
359 interaction of a fossil EPB with an electrified MSTID over  $13.3^\circ$  S. After interaction with the  
360 MSTID, concerned fossil EPB merged with other four EPBs, developed poleward and  
361 bifurcated. Using detrended TEC data, Takahashi et al. (2021) studied the LSWS over Latin  
362 America and found them to be effective in seeding EPBs.

363

## 364 **5 Summary**

365 We present, here, airglow imaging observations of fossil plasma depletions that revived  
366 afresh under the action of prolonged GW activity and became active depletions. Such  
367 simultaneous imaging of thermospheric GWs and depletions was recorded in the ASAI of OI  
368 630 nm emission over Ranchi (mlat.  $\sim 19^\circ$  N), India, on 16 April 2012. Salient features of the  
369 present study are as under:

- 370 1. First, airglow images showed EW-aligned and SN-propagating GWs ( $\lambda \sim 210$  km,  $v$   
371  $\sim 64$  m/s, and  $\tau \sim 0.91$  h) over Ranchi during 1715-1906 UT. Similar GWs were, also,  
372 seen in TEC measurements over a lower latitude station Hyderabad.
- 373 2. A co-existing and prominent fossil depletion DP1 revived under this GW activity  
374 wherein its apex raised from 600 km to  $>800$  km, and the level of intensity depletion  
375 increased from 17 % to 50 %. Another fossil depletion DP2, too, revived.  
376 Interestingly, GWs phase fronts were transverse to the geomagnetic field lines, yet  
377 two fossil depletions revived under their influence and became active depletions.
- 378 3. As GWs phase speed ( $v \sim 64-67$  m/s) nearly matched the eastward drift of depletion  
379 DP1 ( $v \sim 59-70$  m/s), we conjecture that the GWs-driven revival of these fossil  
380 depletions possibly occurred via the spatial resonance mechanism.
- 381 4. An uneven region of increased thickness existed on the southern half of the revived  
382 depletion DP1, wherein some airglow enhancement was seen later in the inner edge of  
383 its west wall. Possibly the gradual disappearance of its southern fraction occurred  
384 because of the intrusion of ambient plasma across the west wall.

385

386 Contrary to the current understanding, this study shows that the GWs fronts aligned  
387 perpendicular to the geomagnetic field lines can effectively grow irregularities. Present  
388 observations of the GWs-driven revival of fossil airglow depletions further contribute to our  
389 understanding of their generation mechanism around midnight.

390

391

392 **Data Availability.** Airglow data used in the present study are available through the  
393 institutional data repository (<http://www.iigm.res.in/>) or  
394 <https://doi.org/10.5281/zenodo.8143215>. Movie created from all-sky 630 nm nightglow  
395 images showing the gravity wave activity and the evolution of depletion DP1 and DP2 is  
396 available from <https://doi.org/10.5281/zenodo.8358134>. Calibrated TEC data is available  
397 from <https://t-ict4d.ictp.it/nequick2/gnss-tec-calibration>.

398

399

400 **Author contributions.** NP conceptualized the research problem and prepared the first draft.  
401 All authors contributed to the interpretation of results, discussion, and subsequent drafting of  
402 the manuscript.

403

404

405 **Acknowledgements:** Funds for Airglow Research at *Indian Institute of Geomagnetism* are  
406 being provided by *Department of Science and Technology (DST), Govt. of India, New*  
407 *Delhi*. GNSS TEC Calibrated data were downloaded from [https://t-](https://t-ict4d.ictp.it/nequick2/gnss-tec-calibration)  
408 [ict4d.ictp.it/nequick2/gnss-tec-calibration](https://t-ict4d.ictp.it/nequick2/gnss-tec-calibration) and *Telecommunications/ICT for Development*  
409 *(T/ICT4D) Laboratory of the Abdus Salam International Centre for Theoretical Physics,*  
410 *Trieste, Italy* is gratefully acknowledged. *SP* is grateful to *Director, Indian Institute of*  
411 *Geomagnetism, Navi Mumbai* for the award of Research Scholarship. Authors sincerely  
412 thank the Editor and Reviewers for their encouragement and critical comments.

413

414

415 **References:**

416 Abdu, M., Iyer, K. N., de Medeiros, R., Batista, I. S. and Sobral, J. H.: Thermospheric  
417 meridional wind control of equatorial spread F and evening prereversal electric field,  
418 *Geophys. Res. Lett.* 33 (7). <http://dx.doi.org/10.1029/2005GL024835>, 2006.

419

420 Abdu, M. A., Kherani, E. A., Batista, I. S., de Paula, E. R., Fritts, D. C., and Sobral, J. H.:  
421 Gravity wave initiation of equatorial spread F/plasma bubble irregularities based on  
422 observational data from the SpreadFEx campaign, *Ann. Geophys.*, 27, 2607-2622.  
423 <https://doi.org/10.5194/angeo-27-2607-2009>, 2009.

424

425 Azeem, I., and Barlage, M.: Atmosphere-ionosphere coupling from convectively generated  
426 gravity waves. *Adv. Space Res.*, 61(7), 1931-1941. <https://doi.org/10.1016/j.asr.2017.09.029>,  
427 2018.

428

429 Ciruolo, L., Azpilicueta, F., Brunini, C., Meza, A. and Radicella, S. M.: Calibration errors on  
430 experimental slant total electron content (TEC) determined with GPS. *J. Geod.*, 81, 111–120,  
431 <https://doi.org/10.1007/s00190-006-0093-1>, 2007.

432

433 Chapagain, N. P., Taylor, M. J., and Eccles, J. V.: Airglow observations and modeling of F  
434 region depletion zonal velocities over Christmas Island, *J. Geophys. Res.*, 116, A02301,  
435 <https://doi.org/10.1029/2010JA015958>, 2011.

436

437 Devasia, C., Jyoti, N., Subbarao, K., Viswanathan, K., Tiwari, D. and Sridharan, R.: On the  
438 plausible linkage of thermospheric meridional winds with the equatorial spread F, *J. Atmos.*  
439 *Sol.-Terrest. Phys.* 64 (1), 1–12, [http://dx.doi.org/10.1016/S1364-6826\(01\)00089-X](http://dx.doi.org/10.1016/S1364-6826(01)00089-X), 2002.

440

441 Drob, D. P., Emmert, J. T., Crowley, G., Picone, J. M., Shepherd, G. G., Skinner, W., et al.:  
442 An empirical model of the Earth's horizontal wind fields: HWM07. *J. Geophys. Res.*, 113,  
443 A12304, <https://doi.org/10.1029/2008JA013668>, 2008.

444

445 Fejer, B. G., and Kelley, M. C.: Ionospheric irregularities. *Rev. Geophys.*, 18(2), 401-454,  
446 <https://doi.org/10.1029/RG018i002p00401>, 1980.

447

448 Figueiredo, C. A. O. B., Takahashi, H., Wrasse, C. M., Otsuka, Y., Shiokawa, K., & Barros,  
449 D.: Medium-scale traveling ionospheric disturbances observed by detrended total electron  
450 content maps over Brazil. *Journal of Geophysical Research: Space Physics*, 123, 2215–2227.  
451 <https://doi.org/10.1002/2017JA025021>, 2018.

452

453 Ford, E. A. K., Aruliah, A. L., Griffin, E. M., and McWhirter, I.: Thermospheric gravity  
454 waves in Fabry-Perot Interferometer measurements of the 630.0nm OI line, *Ann. Geophys.*,  
455 24, 555–566, <https://doi.org/10.5194/angeo-24-555-2006>, 2006.

456

457 Ford, E. A. K., Aruliah, A. L., Griffin, E. M., and McWhirter, I.: Statistical analysis of  
458 thermospheric gravity waves from Fabry-Perot Interferometer measurements of atomic  
459 oxygen, *Ann. Geophys.*, 26, 29–45, <https://doi.org/10.5194/angeo-26-29-2008>, 2008.

460

461 Fritts, D. C., and Alexander, M. J.: Gravity wave dynamics and effects in the middle  
462 atmosphere, *Rev. Geophys.*, 41, 1003, <https://doi.org/10.1029/2001RG000106>, 2003.

463

464 Fritts, D. C., Abdu, M. A., Batista, B. R., Batista, I. S., Batista, P. P., Buriti, R., Clemesha, B.  
465 R., Dautermann, T., de Paula, E. R., Fechine, B. J., Fejer, B. G., Gobbi, D., Haase, J.,  
466 Kamalabadi, F., Kherani, E. A., Laughman, B., Lima, P. P., Liu, H.-L., Medeiros, A., Pautet,  
467 P.-D., Riggan, D. M., Rodrigues, F. S., São Sabbas, F., Sobral, J. H. A., Stamus, P.,  
468 Takahashi, H., Taylor, M. J., Vadas, S. L., Vargas, F., and Wrasse, C. M.: Overview and  
469 summary of the Spread F Experiment (SpreadFEx), *Ann. Geophys.*, 27, 2141–2155,  
470 <https://doi.org/10.5194/angeo-27-2141-2009>, 2009.

471

472 Fukushima, D., Shiokawa, K., Otsuka, Y., and Ogawa, T.: Observation of equatorial  
473 nighttime medium-scale traveling ionospheric disturbances in 630-nm airglow images over 7  
474 years. *J. Geophys. Res.*, 117, A10324. <https://doi.org/10.1029/2012JA017758>, 2012.

475

476 Garcia, F. J., Taylor, M. J., and Kelley, M. C.: Two-dimensional spectra analysis of  
477 mesospheric airglow image data. *Appl. Opt.*, 36(29), 7374-7385.  
478 <https://doi.org/10.1364/AO.36.007374>, 1997.

479

480 Heale, C. J., Inchin, P. A., and Snively, J. B.: Primary versus secondary gravity wave  
481 responses at F-region heights generated by a convective source, *J. Geophys. Res. Space*  
482 *Physics*, 127, e2021JA029947, <https://doi.org/10.1029/2021JA029947>, 2022.

483

484 Huang, C.-S., Kelley, M. C., and Hysell, D. L.: Nonlinear Rayleigh-Taylor instabilities,  
485 atmospheric gravity waves and equatorial spread F, *J. Geophys. Res.*, 98(A9), 15631-15642,  
486 <https://doi.org/10.1029/93JA00762>, 1993.

487  
488 Huang, C.-S., and Kelley, M. C.: Nonlinear evolution of equatorial spread F: 1. On the role of  
489 plasma instabilities and spatial resonance associated with gravity wave seeding, *J. Geophys.*  
490 *Res.*, 101(A1), 283-292, <https://doi.org/10.1029/95JA02211>, 1996.  
491  
492 Huba, J. D., and Joyce, G.: Equatorial spread F modeling: Multiple bifurcated structures,  
493 secondary instabilities, large density ‘bite-outs’ and supersonic flows. *Geophys. Res. Lett.*,  
494 34, L07105. <https://doi.org/10.1029/2006GL028519>, 2007.  
495  
496 Huba, J. D., Joyce, G., and Krall, J.: Three-dimensional equatorial spread F modeling,  
497 *Geophys. Res. Lett.*, 35, L10102. <https://doi.org/10.1029/2008GL033509>, 2008.  
498  
499 Huba, J. D., and Joyce, G.: Global modeling of equatorial plasma bubbles, *Geophys. Res.*  
500 *Lett.*, 37, L17104, <https://doi.org/10.1029/2010GL044281>, 2010.  
501  
502 Huba, J. D., and Krall, J.: Impact of meridional winds on equatorial spread F: Revisited,  
503 *Geophys. Res. Lett.*, 40, 1268– 1272, doi:10.1002/grl.50292, 2013.  
504  
505 Huba, J. D., Drob, D. P., Wu, T.-W., and Makela, J. J.: Modeling the ionospheric impact of  
506 tsunami-driven gravity waves with SAMI3: Conjugate effects. *Geophys. Res. Lett.*, 42,  
507 5719–5726. <https://doi.org/10.1002/2015GL064871>, 2015.  
508  
509 Huba, J. D., and Liu, H.-L.: Global modeling of equatorial spread F with SAMI3/WACCM-  
510 X. *Geophys. Res. Lett.*, 47, e2020GL088258. <https://doi.org/10.1029/2020GL088258>, 2020.  
511  
512 Hysell, D. L., Kelley, M. C., Swartz, W. E., and Woodman, R. F.: Seeding and layering of  
513 equatorial spread F by gravity waves. *J. Geophys. Res.*, 95(A10), 17,253-17,260.  
514 <https://doi.org/10.1029/JA095iA10p17253>, 1990.  
515  
516 Hysell, D. L., Jafari, R., Fritts, D. C., and Laughman, B.: Gravity wave effects on postsunset  
517 equatorial F region stability, *J. Geophys. Res. Space Physics*, 119, 5847– 5860,  
518 doi:10.1002/2014JA019990, 2014.  
519



520 Kelley, M. C., Larsen, M. F., LaHoz, C., and McClure, J. P.: Gravity wave initiation of  
521 equatorial spread F: A case study, *J. Geophys. Res.*, 86 (A11), 9087-9100,  
522 <https://doi.org/10.1029/JA086iA11p09087>, 1981.

523

524 Kelley, M. C.: *The Earth's ionosphere: Plasma physics and electrodynamics* (2nd ed.).  
525 Burlington, MA: Elsevier, 2009.

526

527 Klausner, V., Fagundes, P. R., Sahai, Y., Wrasse, C. M., Pillat, V. G., and Becker-Guedes, F.:  
528 Observations of GW/TID oscillations in the F2 layer at low latitude during high and low solar  
529 activity, geomagnetic quiet and disturbed periods, *J. Geophys. Res.*, 114, A02313,  
530 <https://doi.org/10.1029/2008JA013448>, 2009.

531

532 Krall, J., Huba, J. D., Ossakow, S. L., Joyce, G., Makela, J. J., Miller, E. S., and Kelley, M.  
533 C.: Modeling of equatorial plasma bubbles triggered by non-equatorial traveling ionospheric  
534 disturbances. *Geophys. Res. Lett.*, 38(8), L08103. <https://doi.org/10.1029/2011GL046890>,  
535 2011.

536

537 Krall, J., Huba, J. D., and Fritts, D. C.: On the seeding of equatorial spread F by gravity  
538 waves, *Geophys. Res. Lett.*, 40, 661-664, <https://doi.org/10.1002/grl.50144>, 2013.

539

540 Makela, J. J., Ledvina, B. M., Kelley, M. C. and Kintner, P. M: Analysis of the seasonal  
541 variations of equatorial plasma bubble occurrence observed from Haleakala, Hawaii, *Ann.*  
542 *Geophys.*, 22, 3109-3121, <https://doi.org/10.5194/angeo-22-3109-2004>, 2004.

543

544 Makela, J. J., Kelley, M. C., and Nicolls, M. J.: Optical observations of the development of  
545 secondary instabilities on the eastern wall of an equatorial plasma bubble. *J. Geophys. Res.*,  
546 111, A09311, <https://doi.org/10.1029/2006JA011646>, 2006.

547

548 Makela, J. J., Lognonne, P., Hebert, H., Gehrels, T., Rolland, L., Allgeyer, S., et al.: Imaging  
549 and modeling the ionospheric airglow response over Hawaii to the tsunami generated by the  
550 Tohoku earthquake of 11 March 2011. *Geophys. Res. Lett.*, 38, L00G02.  
551 <https://doi.org/10.1029/2011GL047860>, 2011.

552

553 Makela, J. J., and Otsuka, Y.: Overview of nighttime ionospheric instabilities at low- and  
554 mid-latitudes: Coupling aspects resulting in structuring at the mesoscale. *Space Sci. Rev.*,  
555 168(1-4), 419-440. <https://doi.org/10.1007/s11214-011-9816-6>, 2012.  
556

557 Maruyama, T.: A diagnostic model for equatorial spread F: 1. Model description and  
558 application to electric field and neutral wind effects, *J. Geophys. Res.*, 93 (A12), 14611–  
559 14622. <http://dx.doi.org/10.1029/JA093iA12p14611>, 1988.  
560

561 Maurya, A. K., Parihar, N., Dube, A., Singh, R., Kumar, S., Chanrion, O., Tomicic, M., and  
562 Neubert, T.: Rare observations of sprites and gravity waves supporting D, E, F-regions  
563 ionospheric coupling, *Sci. Rep.*, 12, 581. <https://doi.org/10.1038/s41598-021-03808-5>, 2022.  
564

565 Mendillo, M., and Baumgardner, J.: Airglow characteristics of equatorial plasma depletions.  
566 *J. Geophys. Res.*, 87, 7641-7652, <https://doi.org/10.1029/JA087iA09p07641>, 1982.  
567

568 Mendillo, M., Baumgardner, J., Colerico, M., and Nottingham, D.: Imaging science  
569 contributions to equatorial aeronomy: initial results from the MISETA program, *J. Atmos.*  
570 *Terr. Phys.*, 59, 1587-1599, [https://doi.org/10.1016/S1364-6826\(96\)00158-7](https://doi.org/10.1016/S1364-6826(96)00158-7), 1997.  
571

572 Miller, E. S., Makela, J. J., and Kelley, M. C.: Seeding of equatorial plasma depletions by  
573 polarization electric fields from middle latitudes: Experimental evidence, *Geophys. Res.*  
574 *Lett.*, 36, L18105, <https://doi.org/10.1029/2009GL039695>, 2009.  
575

576 Mukherjee, G. K., Pragati Shikha, R., Parihar, N., Ghodpage, R. and Patil, P. T.: Studies of  
577 the wind filtering effect of gravity waves observed at Allahabad (25.45° N, 81.85° E). *Earth*  
578 *Planets Space* 62, 309-318, <https://doi.org/10.5047/eps.2009.11.008>, 2010.  
579

580 Nishioka, M., Otsuka, Y., Shiokawa, K., Tsugawa, T., Effendy, , Supnithi, P., Nagatsuma, T.,  
581 and Murata, K. T.: On post-midnight field-aligned irregularities observed with a 30.8-MHz  
582 radar at a low latitude: Comparison with F-layer altitude near the geomagnetic equator, *J.*  
583 *Geophys. Res.*, 117, A08337, <https://doi.org/10.1029/2012JA017692>, 2012.  
584

585 Otsuka, Y., Shiokawa, K. and Ogawa, T.: Disappearance of equatorial plasma bubble after  
586 interaction with mid-latitude medium-scale traveling ionospheric disturbance, *Geophysical*  
587 *Research Letters*, 39, L14105, <https://doi.org/10.1029/2012GL052286>, 2012.

588

589 Otsuka, Y.: Review of the generation mechanisms of post-midnight irregularities in the  
590 equatorial and low-latitude ionosphere. *Prog. Earth Planet. Sci.* 5, 57.  
591 <https://doi.org/10.1186/s40645-018-0212-7>, 2018.

592

593 Parihar, N., Singh, D., and Gurubaran, S.: A comparison of ground-based hydroxyl airglow  
594 temperatures with SABER/TIMED measurements over 23° N, India, *Ann. Geophys.*, 35,  
595 353–363, <https://doi.org/10.5194/angeo-35-353-2017>, 2017.

596

597 Parihar, N., Radicella, S. M., Nava, B., Migoya-Orue, Y. O., Tiwari, P., and Singh, R.: An  
598 investigation of the ionospheric F region near the EIA crest in India using OI 777.4 and 630.0  
599 nm nightglow observations. *Ann. Geophys.*, 36(3), 809-823. [https://doi.org/10.5194/angeo-](https://doi.org/10.5194/angeo-36-809-2018)  
600 [36-809-2018](https://doi.org/10.5194/angeo-36-809-2018), 2018.

601

602 Parihar, N.: Rare occurrence of off-equatorial edge initiating and equatorward surging plasma  
603 depletions observed in OI 630-nm imaging. *J. Geophys. Res. Space Physics*, 124, 2887-2896.  
604 <https://doi.org/10.1029/2018JA026155>, 2019.

605

606 Paulino, I., Takahashi, H., Medeiros, A. F., Wrasse, C. M., Buriti, R. A., Sobral, J. H. A., and  
607 Gobbi, D.: Mesospheric gravity waves and ionospheric plasma bubbles observed during the  
608 COPEX campaign. *J. Atmos. Sol.-Terr. Phys.*, 73(11-12), 1575-1580.  
609 <https://doi.org/10.1016/j.jastp.2010.12.004>, 2011.

610

611 Paulino, I., Medeiros, A. F., Vadas, S. L., Wrasse, C. M., Takahashi, H., Buriti, R. A., Leite,  
612 D., Filgueira, S., Bageston, J. V., Sobral, J. H. A., and Gobbi, D.: Periodic waves in the lower  
613 thermosphere observed by OI630 nm airglow images, *Ann. Geophys.*, 34, 293-301,  
614 <https://doi.org/10.5194/angeo-34-293-2016>, 2016.

615

616 Paulino, I., Moraes, J. F., Maranhão, G. L., Wrasse, C. M., Buriti, R. A., Medeiros, A. F.,  
617 Paulino, A. R., Takahashi, H., Makela, J. J., Meriwether, J. W., and Campos, J. A. V.:  
618 Intrinsic parameters of periodic waves observed in the OI6300 airglow layer over the

619 Brazilian equatorial region, *Ann. Geophys.*, 36, 265–273, <https://doi.org/10.5194/angeo-36->  
620 265-2018, 2018.

621

622 Pimenta, A. A., Fagundes, P. R., Sahai, Y., Bittencourt, J. A., and Abalde, J. R.: Equatorial F-  
623 region plasma depletion drifts: latitudinal and seasonal variations. *Ann. Geophys.*, 21, 2315-  
624 2322, <https://doi.org/10.5194/angeo-21-2315-2003>, 2003.

625

626 Sau, S., Narayanan, V. L., Gurubaran, S., and Emperumal, K.: Study of wave signatures  
627 observed in thermospheric airglow imaging over the dip equatorial region. *Adv. Space Res.*,  
628 62(7), 1762–1774, <https://doi.org/10.1016/j.asr.2018.06.039>, 2018.

629

630 Sekar, R., Chakrabarty, D., Sarkhel, S., Patra, A. K., Devasia, C. V., and Kelley, M. C.:  
631 Identification of active fossil bubbles based on coordinated VHF radar and airglow  
632 measurements, *Ann. Geophys.*, 25, 2099-2102, <https://doi.org/10.5194/angeo-25-2099-2007>,  
633 2007.

634

635 Shiokawa, K., Otsuka, Y., Lynn, K. J., Wilkinson, P., and Tsugawa, T.: Airglow-imaging  
636 observation of plasma bubble disappearance at geomagnetically conjugate points. *Earth*  
637 *Planets and Space*, 67(1), 43, <https://doi.org/10.1186/s40623-015-0202-6>, 2015.

638

639 Singh, S., Johnson, F. S., and Power, R. A.: Gravity wave seeding of equatorial plasma  
640 bubbles. *J. Geophys. Res.*, 102(A4), 7399– 7410, <https://doi.org/10.1029/96JA03998>, 1997.

641

642 Smith, S. M., Martinis, C. R., Baumgardner, J., and Mendillo, M.: All-sky imaging of  
643 transglobal thermospheric gravity waves generated by the March 2011 Tohoku Earthquake, *J.*  
644 *Geophys. Res. Space Physics*, 120, 10,992-10,999, <https://doi.org/10.1002/2015JA021638>,  
645 2015.

646

647 Sreeja, V., Vineeth, C., Pant, T. K., Ravindran, S. and Sridharan, R.: Role of gravity wavelike  
648 seed perturbations on the triggering of ESF-First results from unique dayglow observations,  
649 *Ann. Geophys.*, 27, 313-318, <https://doi.org/10.5194/angeo-27-313-2009>, 2009.

650

651 Takahashi, H., Taylor, M. J., Pautet, P.-D., Medeiros, A. F., Gobbi, D., Wrasse, C. M.,  
652 Fechine, J., Abdu, M. A., Batista, I. S., Paula, E., Sobral, J. H. A., Arruda, D., Vadas, S. L.,

653 Sabbas, F. S., and Fritts, D. C.: Simultaneous observation of ionospheric plasma bubbles and  
654 mesospheric gravity waves during the SpreadFEx Campaign, *Ann. Geophys.*, 27, 1477-1487,  
655 <https://doi.org/10.5194/angeo-27-1477-2009>, 2009.

656

657 Takahashi, H., Wrasse, C. M., Figueiredo, C. A. O. B., Barros, D., Paulino, I., Essien, P., et  
658 al.: Equatorial plasma bubble occurrence under propagation of MSTID and MLT gravity  
659 waves. *J. Geophys. Res.: Space Physics*, 125, e2019JA027566.  
660 <https://doi.org/10.1029/2019JA027566>, 2020.

661

662 Takahashi, H., Essien, P., Figueiredo, C. A. O. B., Wrasse, C. M., Barros, D., Abdu, M. A.,  
663 Otsuka, Y., Shiokawa, K., and Li, G. Z.: Multi-instrument study of longitudinal wave  
664 structures for plasma bubble seeding in the equatorial ionosphere. *Earth Planet. Phys.*, 5(5),  
665 368–377. <https://doi.org/10.26464/epp2021047>, 2021.

666

667 Taori, A., Makela, J. J., and Taylor, M. J.: Mesospheric wave signatures and equatorial  
668 plasma bubbles: A case study, *J. Geophys. Res.*, 115, A6, A06302,  
669 <https://doi.org/10.1029/2009JA015088>, 2010.

670

671 Taori, A., Jayaraman, A., and Kamalakar, V.: Imaging of mesosphere–thermosphere airglow  
672 emissions over Gadanki (13.5° N, 79.2° E): First results. *J. Atmos. Sol.-Terr. Phys.*, 93, 21-  
673 28. <https://doi.org/10.1016/j.jastp.2012.11.007>, 2013.

674

675 Taori, A., Parihar, N., Ghodpage, R., Dashora, N., Sripathi, S., Kherani, E. A., and Patil, P. T.  
676 (2015). Probing the possible trigger mechanisms of an equatorial plasma bubble event based  
677 on multistation optical data. *J. Geophys. Res. Space Physics*, 120, 8835-8847.  
678 <https://doi.org/10.1002/2015JA021541>.

679

680 Tsunoda, R. T.: On seeding equatorial spread F: Circular gravity waves, *Geophys. Res. Lett.*,  
681 37, L10104, <https://doi.org/10.1029/2010GL043422>, 2010.

682

683 Tulasi Ram, S., Yamamoto, M., Tsunoda, R. T., Chau, H. D., Hoang, T. L., Damtie, B.,  
684 Wassae, M., Yatini, C. Y., Manik, T., and Tsugawa, T.: Characteristics of large-scale wave  
685 structure observed from African and Southeast Asian longitudinal sectors, *J. Geophys. Res.*  
686 *Space Physics*, 119, 2288-2297, <https://doi.org/10.1002/2013JA019712>, 2014.

687

688 Vadas, S. L., and Azeem, I.: Concentric secondary gravity waves in the thermosphere and  
689 ionosphere over the continental United States on 25-26 march 2015 from deep convection. *J.*  
690 *Geophys. Res. Space Physics*, 126, e2020JA028275. <https://doi.org/10.1029/2020JA028275>,  
691 2021.

692

693 Wrasse, C. M., Figueiredo, C. A. O. B., Barros, D., Takahashi, H., Carrasco, A. J., Vital, L.  
694 F. R., Rezende, L. C. A., Egito, F., Rosa, G. M., and Sampaio, A. H. R.: Interaction between  
695 Equatorial Plasma Bubbles and a Medium-Scale Traveling Ionospheric Disturbance,  
696 observed by OI 630 nm airglow imaging at Bom Jesus de Lapa, Brazil. *Earth Planet. Phys.*,  
697 5(5), 397–406. <https://doi.org/10.26464/epp2021045>, 2021.

698

699 Woodman, R. F.: Spread F: An old equatorial aeronomy problem finally resolved? *Ann.*  
700 *Geophys.*, 27(5), 1915-1934. <https://doi.org/10.5194/angeo-27-1915-2009>, 2009.

701

702 Yadav, S., Sridharan, R., Sunda, S. and Pant, T. K.: Further refinements to the spatiotemporal  
703 forecast model for L-band scintillation based on comparison with C/NOFS observations, *J.*  
704 *Geophys. Res. Space Physics*, 122, 5643-5652, <https://doi.org/10.1002/2017JA023869>, 2017.

705

706 Zalesak, S., and Ossakow, S.: Nonlinear equatorial spread F: Spatially large bubbles resulting  
707 from large horizontal scale initial perturbations. *J. Geophys. Res.*, 85(A5), 2131-2142.  
708 <https://doi.org/10.1029/JA085iA05p02131>, 1980.

709

710 **Figure Captions**

711 **Figure 1.** ASAI images during 1742-1830 UT over Ranchi ( $23.3^\circ$  N,  $85.3^\circ$  E, mlat.  $\sim 19^\circ$  N)  
712 on 16 April 2012. DP1 is the first fossil plasma depletion that showed GWs driven revival.  
713 Depletions OD1 and OD2 preceded depletion DP1. ROI1 is the region-of-interest wherein the  
714 south-north propagating GW activity and faint signatures of eastward drifting depletion DP1  
715 were seen initially. Some weakly noticeable GWs fronts are 'f1', 'f2' and 'f3' (in  
716 succession). 't1' and 't2' are trough that precede fronts 'f1' and 'f2', respectively. 'S1' and  
717 'S2' are the fractions of fronts 'f1' and 'f2', respectively, that subsequently got linked to the  
718 west wall of depletion DP1.

719  
720 **Figure 2.** Same as Figure 1 but for 1836-1942 UT. DP2 is the second fossil depletion that  
721 showed GWs driven revival. Some noticeable GWs fronts are 'f3' and 'f4'. A1 and A2 are  
722 two arc-shaped regions of airglow enhancement near the east and west wall of depletion DP1.  
723 ROI2 is the region-of-interest wherein ambient plasma diffusion occurred across the west  
724 wall of depletions DP1.

725  
726 **Figure 3.** Typical time difference ASAI of OI 630 nm emission over Ranchi showing GW  
727 activity during 1742–1830 UT.

728  
729 **Figure 4.** (a)-(b) North-south (NS) keogram along  $84.4^\circ$  E and  $85.3^\circ$  E longitude generated  
730 from OI 630 nm images during 1730-1930 UT. Alternating bright and dark intensity  
731 striations (i.e. wave traces) can be seen over North. Probably depletions masked GWs  
732 features over South, and hence, these wave traces were not seen. Slope of these striations  
733 indicates towards the south-north movement of GW fronts. A few clear wave traces that were  
734 used to estimate speed of GWs are marked by black arrow as 'b1', 'b2', 'b3' and 'b4'.

735  
736 **Figure 5.** (a) Scatter plot of the TEC along the track of IPPs for a few GPS satellites over  
737 Hyderabad ( $17.3^\circ$  N,  $78.6^\circ$  E, mlat.  $\sim 12.0^\circ$  N) during 1630-1930 UT on 16 April 2012. PRN  
738 numbers of GPS satellites along with the start time at 1700 UT are marked adjacent to the  
739 corresponding IPPs trajectory. G28's trajectory lay close to the south-west sector of the  
740 ASAI. Imager's field-of-view is shown by dashed quarter circle with its centre at Ranchi. (b)  
741 TEC variations of a few satellites showing the presence of GWs activity.

742

743 **Figure 6.** Selected ASAI images showing the revival of fossil depletion **DP3** during 1730-  
744 1854 UT on 06 March 2013 over Ranchi. **ROI3** is the region-of-interest wherein depletion  
745 **DP3** appeared sliced by an unclear thin streak of slightly enhanced airglow. **BR1** and **BR2**  
746 are two structuring that developed on its east wall.

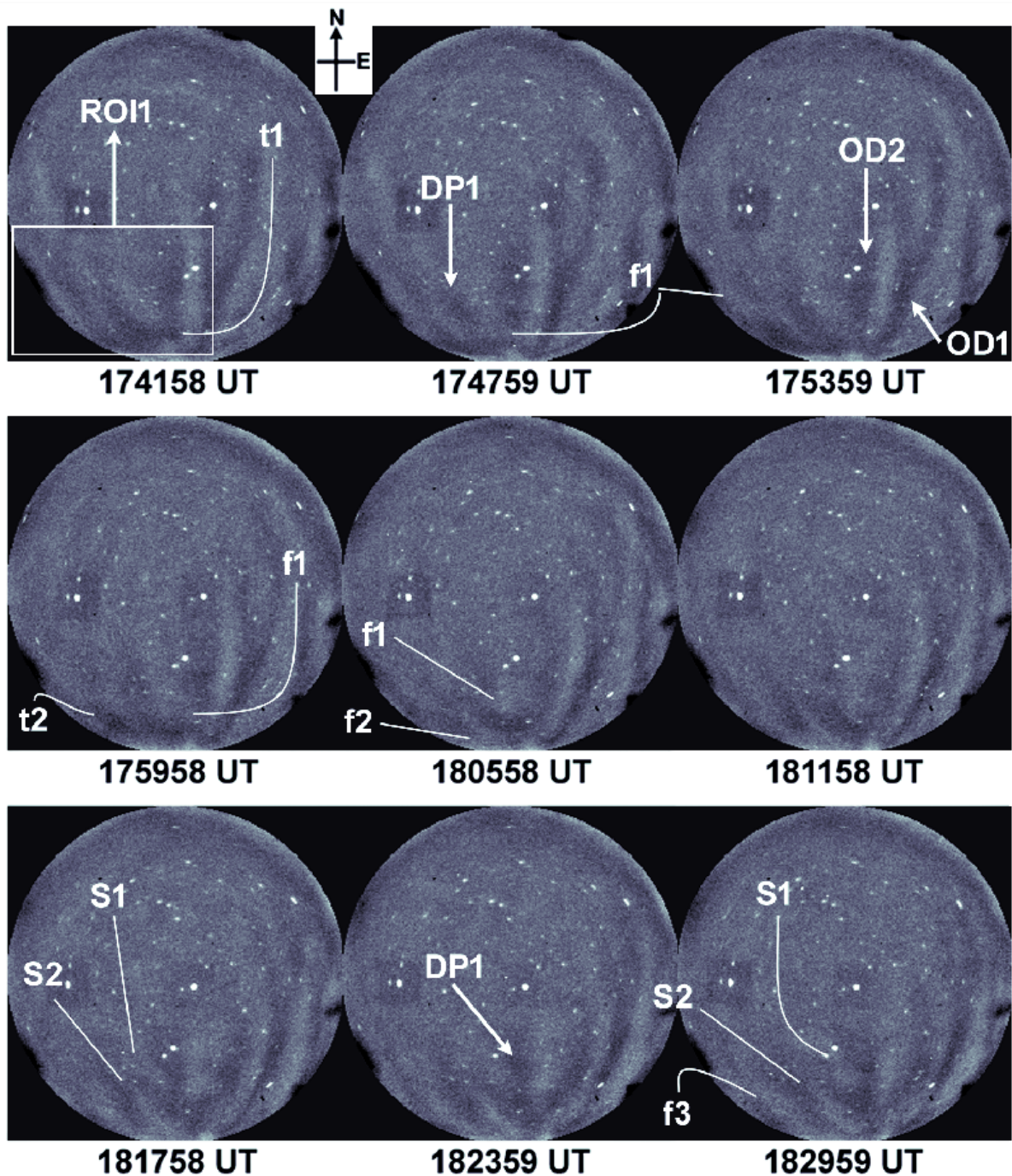
747

748 **Figure 7.** Limited time difference ASAI images showing GW activity during 1530-1700 UT  
749 on 06 March 2013. Beginning 1336 UT, GW signatures were seen in airglow images;  
750 however, activity intensified during 1530-1736 UT. Some of clear GW fronts are marked as  
751 'g1', 'h1' and 'k1'.

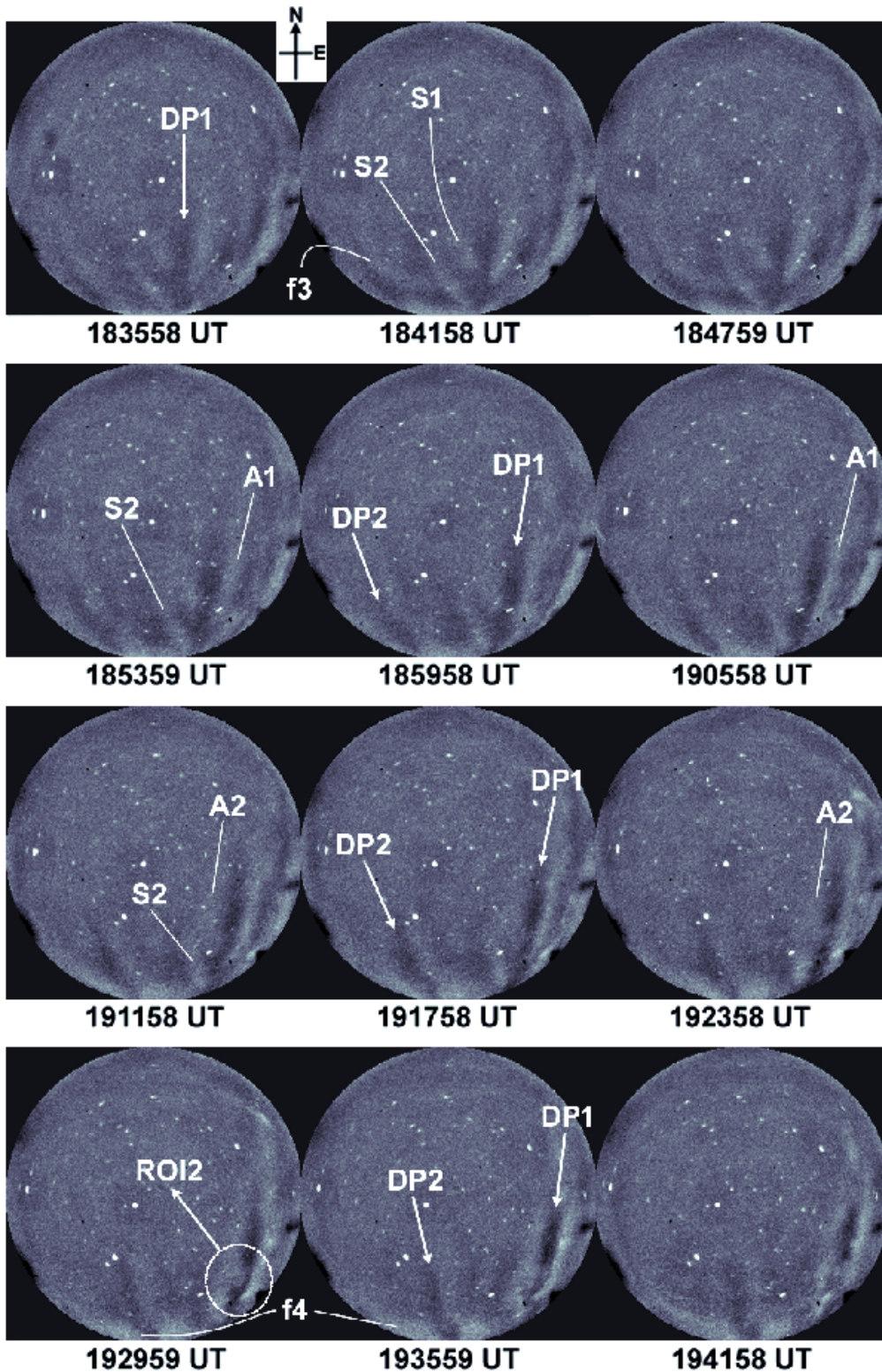
752

753

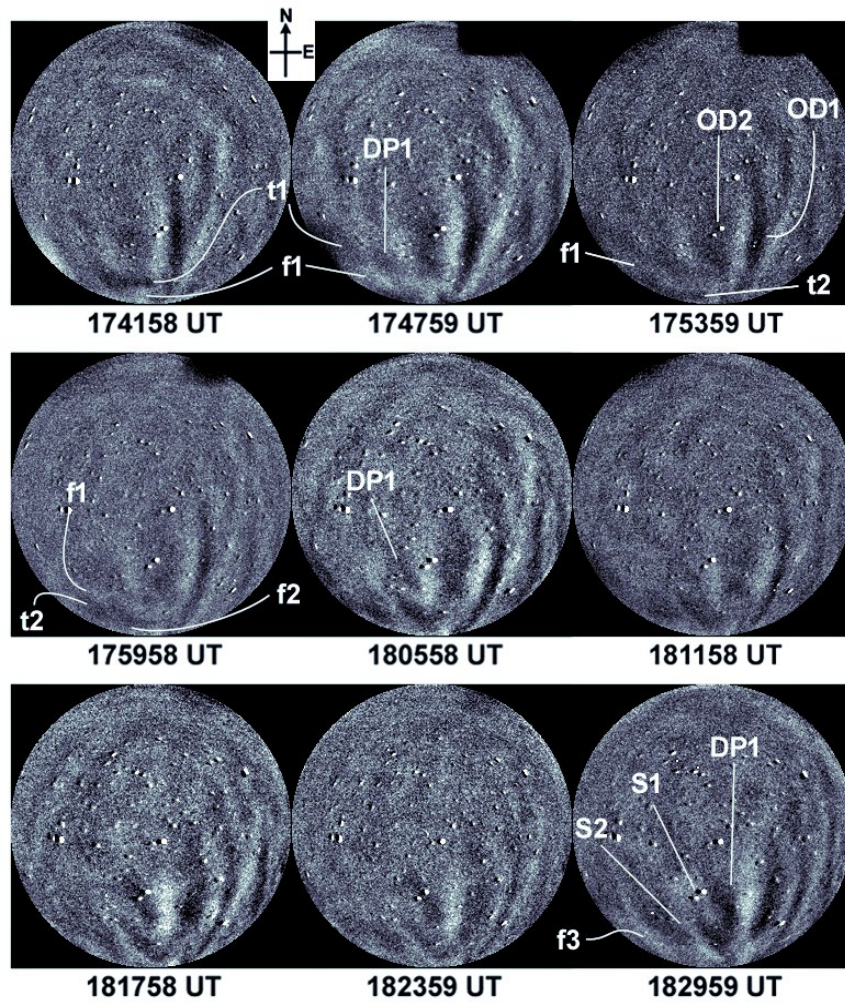




754  
 755 **Figure 1.** ASAI images during 1742-1830 UT over Ranchi (23.3° N, 85.3° E, mlat. ~19° N)  
 756 on 16 April 2012. DP1 is the first fossil plasma depletion that showed GWs driven revival.  
 757 Depletions OD1 and OD2 preceded depletion DP1. ROI1 is the region-of-interest wherein the  
 758 south-north propagating GW activity and faint signatures of eastward drifting depletion DP1  
 759 were seen initially. Some weakly noticeable GWs fronts are 'f1', 'f2' and 'f3' (in  
 760 succession). 't1' and 't2' are trough that precede fronts 'f1' and 'f2', respectively. 'S1' and  
 761 'S2' are the fractions of fronts 'f1' and 'f2', respectively, that subsequently got linked to the  
 762 west wall of depletion DP1.

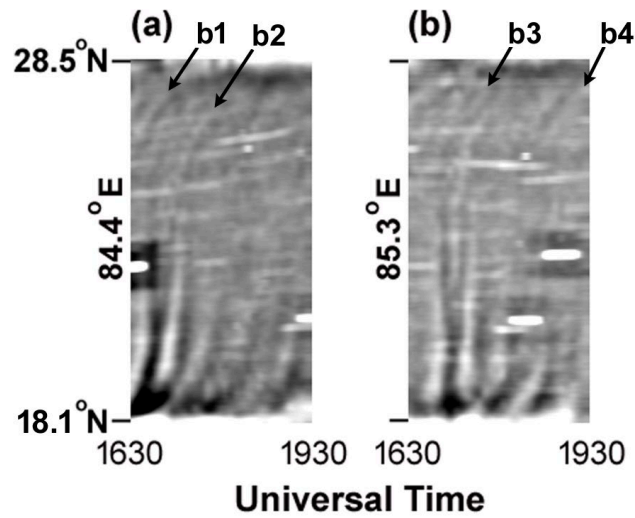


763  
 764 **Figure 2.** Same as Figure 1 but for 1836-1942 UT. DP2 is the second fossil depletion that  
 765 showed GWs driven revival. Some noticeable GWs fronts are 'f3' and 'f4'. A1 and A2 are  
 766 two arc-shaped regions of airglow enhancement near the east and west wall of depletion DP1.  
 767 ROI2 is the region-of-interest wherein ambient plasma diffusion occurred across the west  
 768 wall of depletions DP1.



769

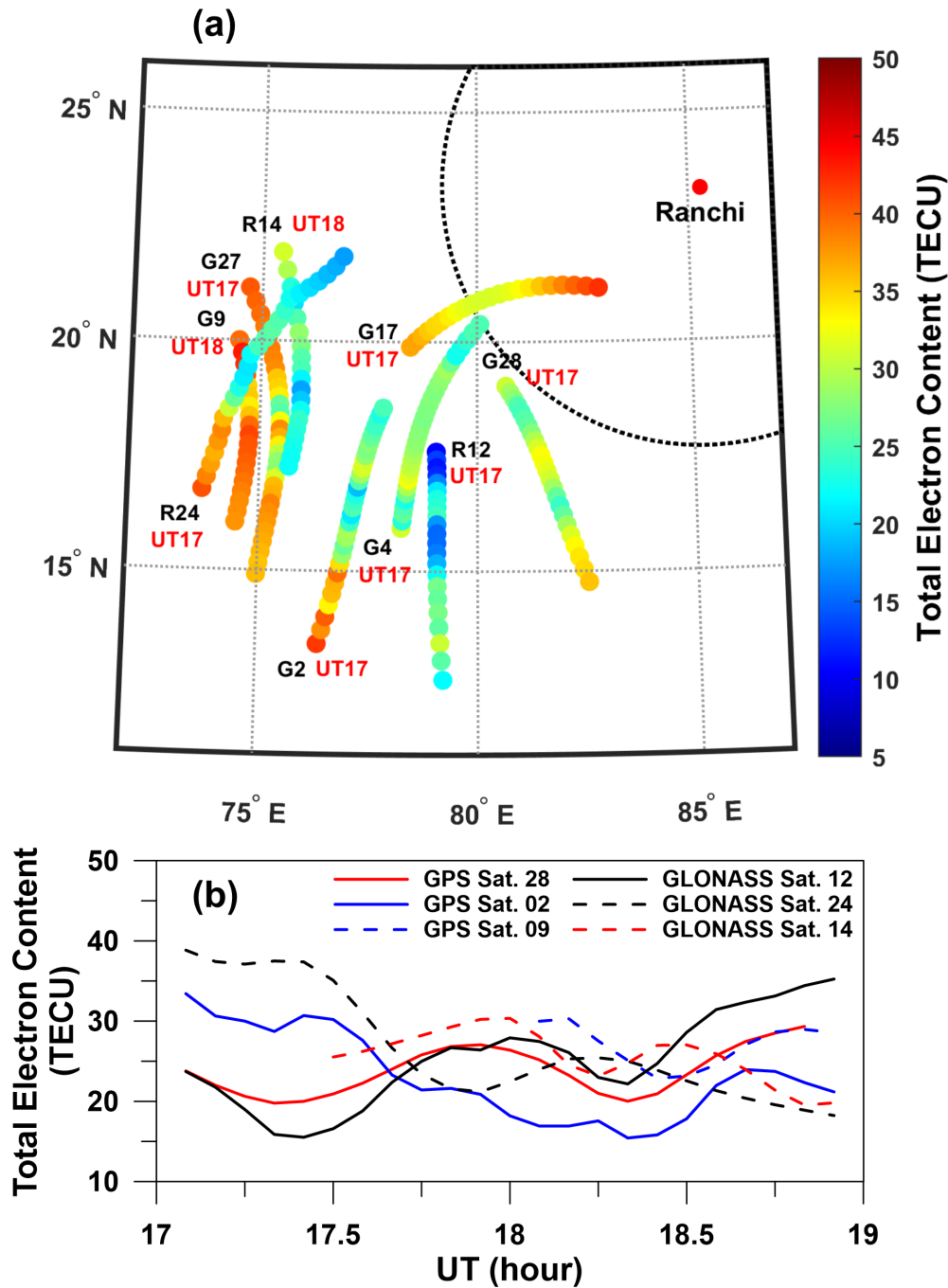
770 **Figure 3.** Typical time difference ASAI of OI 630 nm emission over Ranchi showing GW  
 771 activity during 1742–1830 UT.



772

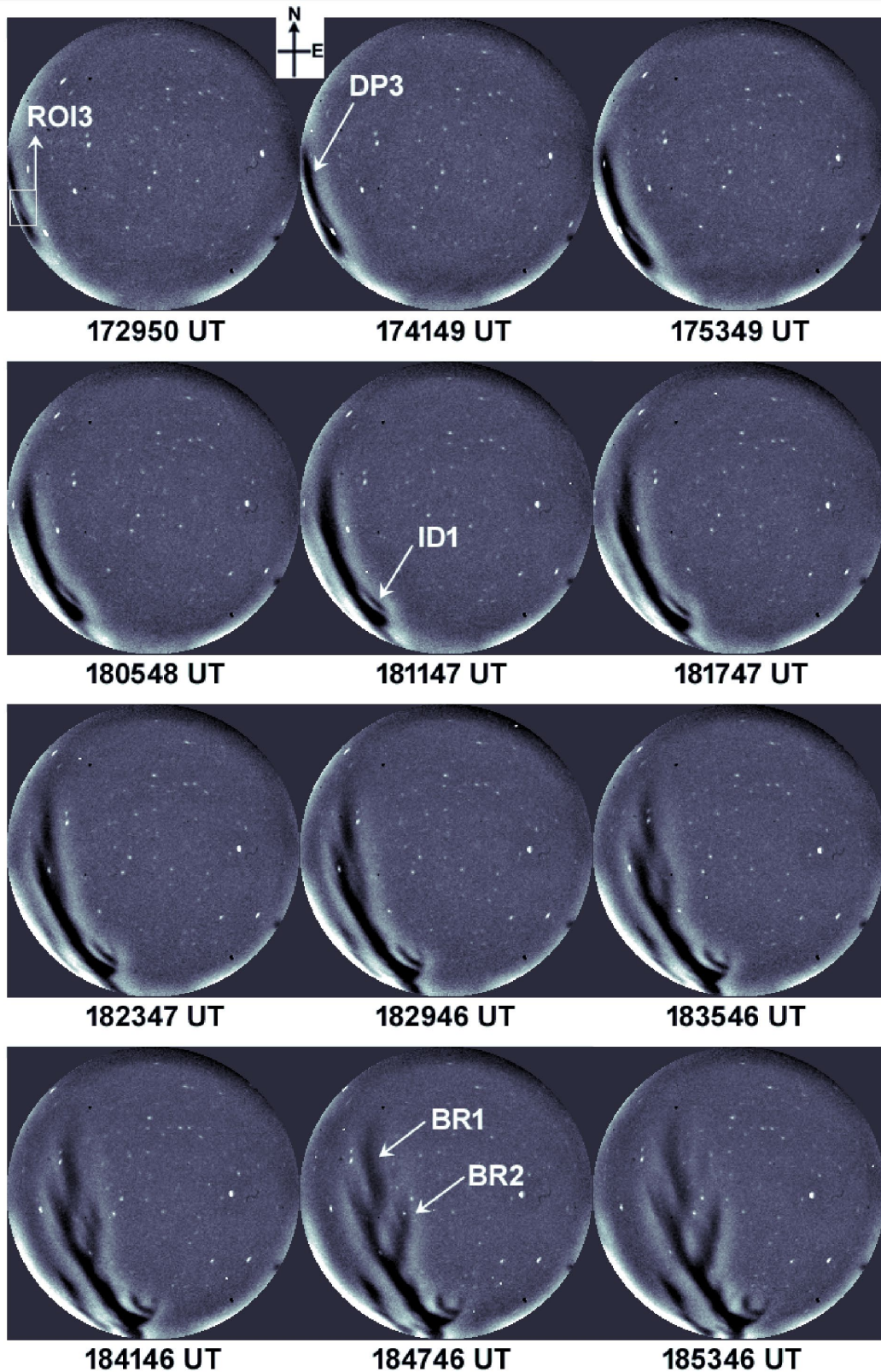
773 **Figure 4.** (a)-(b) North-south (NS) keogram along 84.4° E and 85.3° E longitude generated  
 774 from OI 630 nm images during 1730-1930 UT. Alternating bright and dark intensity  
 775 striations (i.e. wave traces) can be seen over North. Probably depletions masked GWs  
 776 features over South, and hence, these wave traces were not seen. Slope of these striations  
 777 indicates towards the south-north movement of GW fronts. A few clear wave traces that were  
 778 used to estimate speed of GWs are marked by black arrow as 'b1', 'b2', 'b3' and 'b4'.

779



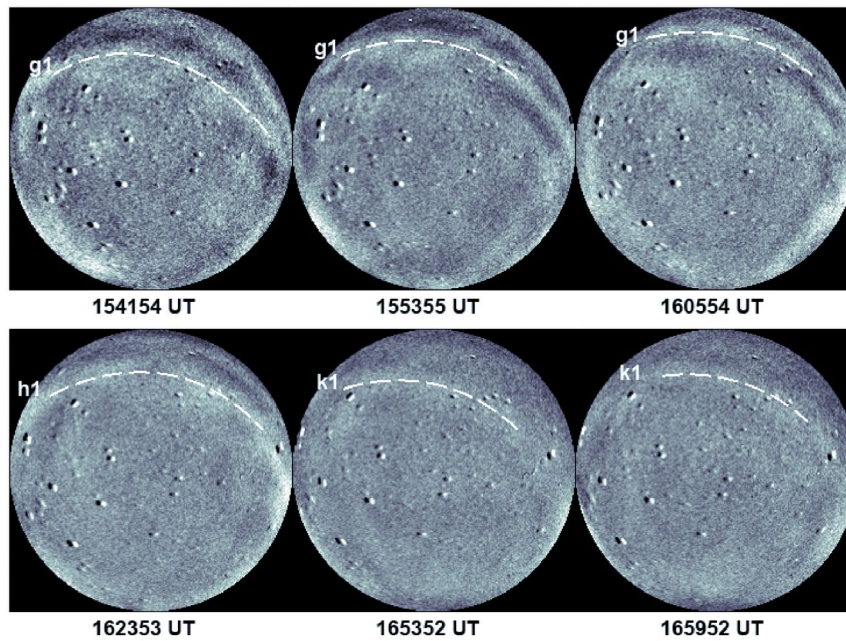
780  
781  
782  
783  
784  
785  
786  
787

**Figure 5.** (a) Scatter plot of the TEC along the track of IPPs for a few GPS and GLONASS satellites (prefixed as ‘G’ and ‘R’, respectively) in the geographic grid of 5-35° N x 65-95° E during 1630-1930 UT on 16 April 2012. PRN numbers of GPS/GLONASS satellites along with the start time at 1700 UT are marked adjacent to the corresponding IPPs trajectory. G28’s trajectory lay close to the south-west sector of the ASAI. Imager’s field-of-view is shown by dashed quarter circle with its centre at Ranchi. (b) TEC variations of a few GPS/GLONASS satellites showing the presence of GWs activity.



788  
789  
790  
791  
792

**Figure 6.** Selected ASAI images showing the revival of fossil depletion **DP3** during 1730-1854 UT on 06 March 2013 over Ranchi. **ROI3** is the region-of-interest wherein depletion **DP3** appeared sliced by an unclear thin streak of slightly enhanced airglow. **BR1** and **BR2** are two structuring that developed on its east wall.



794

795 **Figure 7.** Limited time difference ASAI images showing GW activity during 1530-1700 UT  
796 on 06 March 2013. Beginning 1336 UT, GW signatures were seen in airglow images;  
797 however, activity intensified during 1530-1736 UT. Some of clear GW fronts are marked as  
798 'g1', 'h1' and 'k1'.

799 **Supplementary Material**

800 **Supplementary Material S1:** Movie created from all-sky 630 nm nightglow images  
801 showing the gravity wave activity and the evolution of depletion DP1 and DP2 (available  
802 from <https://doi.org/10.5281/zenodo.8358134>).